Mechanism studies for relativistic attosecond electron bunches from laser-illuminated nanotargets

F. Tan,[1] S. Y. Wang,[1] Y. X. Zhang,[2] Z. M. Zhang,[1] B. Zhu,[1] Y. C. Wu,[1] M. H. Yu,[1] Y. Yang,[1] G. li,[1] T. K. Zhang,[1] Y. H. Yan,[1] F. Lu,[1] W. Fan,[1] W. M. Zhou,[1] Y. Q. Gu,[3,*] and B. Qiao[4,†]

[1]*Science and Technology on Plasma Physics Laboratory, Research Center of Laser Fusion, China Academy of Engineering Physics, Mianyang 621900, China*

[2]*Department of Experimental Physics, Research Center of Laser Fusion, China Academy of Engineering Physics, Mianyang 621900, China*

[3]*National Key Laboratory of Plasma Physics, Laser Fusion Research Center, China Academy of Engineering Physics, Mianyang 621900, China*

[4]*Center for Applied physics and Techology, Peking University, Beijing 100871, China*

(Received 5 July 2023; accepted 5 December 2023; published 12 April 2024)

To find a way to control the electron-bunching process and the bunch-emitting directions when an ultraintense, linearly polarized laser pulse interacts with a nanoscale target, we explored the mechanisms for the periodical generation of relativistic attosecond electron bunches. By comparing the simulation results of three different target geometries, the results show that for nanofoil target, limiting the transverse target size to a small value and increasing the longitudinal size to a certain extent is an effective way to improve the total electron quantity in a single bunch. Then the subfemtosecond electronic dynamics when an ultrashort ultraintense laser grazing propagates along a nanofoil target was analyzed through particle-in-cell simulations and semiclassical analyses, which shows the detailed dynamics of the electron acceleration, radiation, and bunching process in the laser field. The analyses also show that the charge separation field produced by the ions plays a key role in the generation of electron bunches, which can be used to control the quantity of the corresponding attosecond radiation bunches by adjusting the length of the nanofoil target.

DOI: 10.1103/PhysRevE.109.045205

I. INTRODUCTION

During the interaction of relativistic laser with overdense plasmas, attosecond electron bunches with ultrahigh density can be generated [1–5]. Then through three mechanisms: Coherent wake emission (CWE) [6,7], relativistically oscillation mirror (ROM) [8–15], and coherent synchrotron emission (CSE) [16–19], the electron bunches can generate attosecond pulses with photon energy from extreme ultraviolet to soft x ray [20]. Compared with the harmonic generation in gas targets, there is no limitation on the applicable laser intensity and plasma density. So this kind of harmonic generation may have significantly higher conversion efficiency and harmonic intensity. Such ultrafast ultraintense attosecond source may be applied to many applications, such as nonlinear optics in the extreme ultraviolet region [21], photoelectron spectroscopy [22,23], and ultrafast electronic motion detection [24–30].

When the attosecond source is applied as a detection tool, the way to obtain the isolated pulse, instead of the pulse train, is the most important topic. In the model called attosecond lighthouse [31,32], the rotated laser wave-front leads to the generation of angularly separated attosecond pulses. For the studies using Polarization gating [33], few-cycle laser-plasma interaction [34], two-color field [35], and frequency gating [36], besides the chosen isolated attosecond pulse the generation of other attoseconds pulses can be marked suppressed. Xu's work [37] shows that the establishment of an intense transient electric field using capacitor nano foil target can also restrict the generation of attosecond pulses and lead to isolated attosecond pulses.

In addition, nanoscale mass-limited targets have shown great potential in generating isolated attosecond electron bunches and high-order harmonics. Laser irradiated nanoscale droplets [3,38,39], nanowire [40,41], and nanometric tungsten needles [5] can be used to generate relativistic attosecond electron bunches. However, compared with these in the large-size targets, the electrons in the ionized nanoscale mass-limited targets will be more deeply affected by the highly localized surface electric field generated by the charge separation field of the ions. The proportion of the area affected by the surface electric field in the total volume is much larger for the nanoscale mass-limited targets, so most of the electrons in the mass-limited target will be affected by the surface electric field. Due to the influence of the transverse and longitudinal components of the surface electric field, the electrons will also have transverse and longitudinal initial velocities. Then when the electrons are accelerated in the laser field, the different initial velocities will lead to different emission directions, acceleration process, and finally obtained energy. The electrons with similar initial conditions have similar acceleration trajectories, so they will converge into an electron bunch. Different target sizes will lead to different ranges of

*yqgu@caep.cn
†bqiao@pku.edu.cn

the initial conditions, which determines the number of generated electron bunches. For targets with ultrasmall size, all electrons in the target have similar initial conditions, so they will eventually aggregate into an isolated attosecond electron bunch. However, due to the limited target size, the number of electrons in this bunch is relatively small. To increase the total electron number in one bunch, increasing the target size is a possible way. However, the larger target size may lead to a wider range of the electron initial conditions, which may lead to the generation of multiple electron bunches. Therefore, to suppress the generation of multiple electron beams and improve the electron number in one bunch for nanoscale targets with a larger size, it is necessary to study the influence of different target geometries on the final electron distribution and explore the physical mechanism of electron acceleration in the target surface electric field and laser field.

In the following paragraphs, first we studied the different electron distributions for three different target geometries under the illumination of a relativistic laser pulse. The simulation results show that the increase of the transverse target scale hardly affects the electron quantity in a single electron bunch. Multiple electron bunches will also be generated for a larger transverse target scale. Limiting the transverse size to a smaller value and increasing the longitudinal size to a certain extent can significantly improve the total electron number in a single bunch and control the generation of multiple electron bunches. Next, through PIC simulation and semiclassical analyses, the subfemtosecond electronic dynamics during the generation of attosecond electron bunches are explored. How initial conditions affect the electron trajectories is also studied.

II. THE INFLUENCES OF THE LONGITUDE AND TRANSVERSE TARGET LENGTHS ON THE ELECTRON BUNCH PRODUCTION

To select the target type which is most suitable for producing the electron bunch with the higher electron number, it is necessary to compare the obtained electronic spatial distribution and the total charges in each electron bunch under different target geometries. Therefore, we explored the interactions between a relativistic linearly polarized laser and mass-limited targets with different geometries using the PIC simulation code VORPAL [42]. In the following simulations, an initially ionized target is used. The simulation box has a size of 10λ and 20λ in the XY plane, where λ is the laser wavelength. The spatial resolution is 1,000 cells per λ in X directions and 100 cells per λ in Y directions. The laser is linearly polarized along the Y axis and propagates from the left boundary of the simulation box to right, towards the $+X$ direction. The temporal profile of the laser field is of Gaussian shape with a pulse duration $\sigma = 4\lambda/c$, wavelength $\lambda = 800$ nm, and initial phase $\phi = 0$. The laser beam waist is 2.26 μm. The normalized laser field a_0 is 100. The electron density of the targets is $n_e = 75n_c$, where n_c is the critical density. At $t = 0$, the laser leading edge reaches the left edge of the simulation box. It notes that these laser parameters can be realized for a ~1PW laser facility, which makes the corresponding experiments possible to be conducted on the current laser facilities.

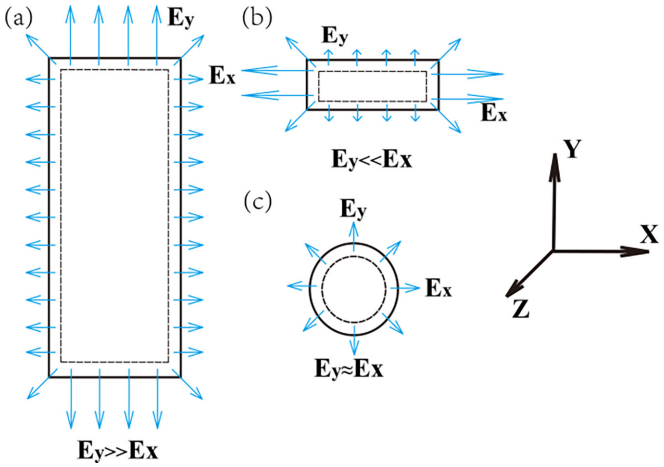

FIG. 1. Three different target geometries used in the simulation.

Three different target geometries shown in Fig. 1 are used in the simulation: (a) the nanofoil target with 20 nm in longitudinal length and changeable transverse length, (b) the nanosphere with changeable diameter, and (c) the nanofoil target with changeable longitudinal length and fixed transverse length of 20 nm. For target geometry (a), the obtained electron distributions under different transverse lengths are shown in Fig. 2. Figures 2(a)–2(c) show that with the increasing of the transverse target length and the kept unchanged longitudinal length, the obtained results change from a single isolated electron bunch to multiple electron bunches.

To evaluate the influence of the target transverse size on the electronic quantity in each electron bunch, the results in Figs. 2(a)–2(c) are summed along the Y axis to obtain the distribution of electronic quantity along the X direction, as shown in Fig. 2(d). Figure 2(d) shows that with the increase of the target transverse size, the leading two peaks just increase

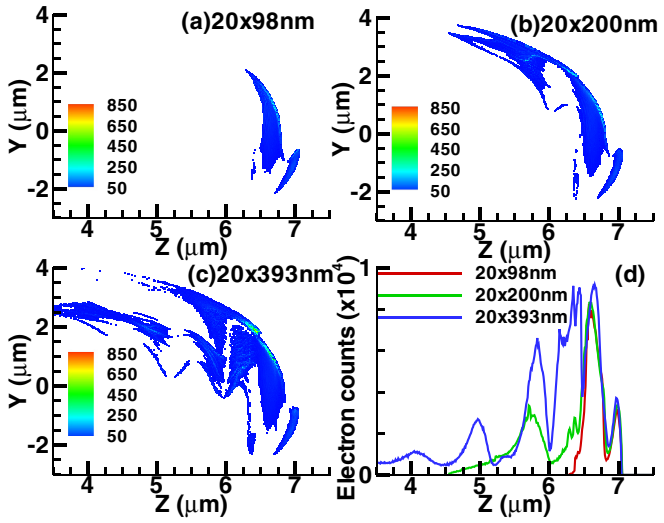

FIG. 2. The spatial distribution of the generated electrons for mass-limited foil target with a different transverse length of (a) 98 nm, (b)200 nm, (c) 393 nm, and (d) the integrated results along the Y axis. The colorbar indicates the value of the electron density with arbitrary units.

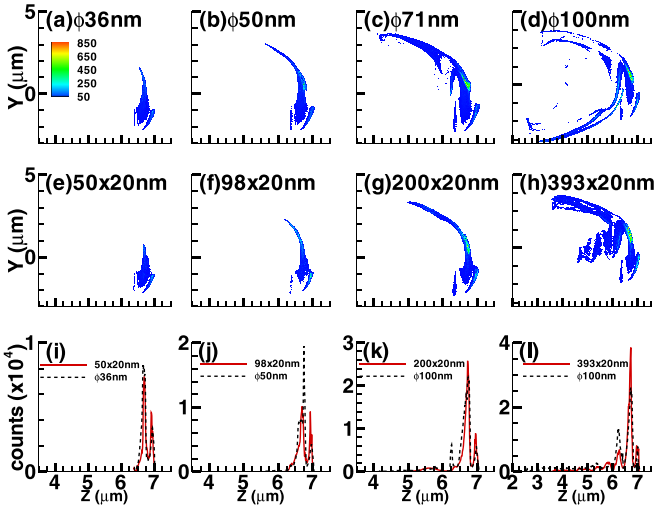

FIG. 3. The spatial distribution of the generated electrons for nanosphere targets with diameters of (a) 36 nm, (b) 50 nm, (c) 71 nm, (d) 100 nm, nanofoil target with changeable longitudinal length of (e) 50 nm, (f) 98 nm, (g) 200 nm, (h) 393 nm, and (i), (j), (k), (l) the corresponding integrated results along the Y axis. The colorbar indicates the value of the electron density with arbitrary units.

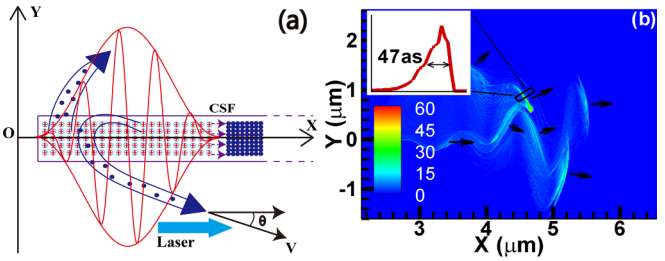

FIG. 4. (a) Schematic drawing of the interaction between the relativistic laser pulse and nanofoil target. The angle from the electron-emitting direction to the $+X$ direction is defined as θ. During the continuous electron ejection from the target, a continuous increasing charge separation field (CSF) is formed. (b) The generated fanlike electron bunches where the black arrows indicate the emitting direction of the bunches. (c) The averaged electron bunch duration drawn from the black rectangle in panel (b). The colorbar indicates the value of the electron density with arbitrary units.

slightly. Meanwhile, new peaks continuously appear. So it is obvious that when the longitudinal size remains unchanged, just increasing the transverse size is not conducive to improving the electronic quantity in a single electron bunch. The adverse consequences also include the evolution from isolated pulse to pulse train.

Next, similar analyses can be conducted for target geometries (2) and (3), as shown in Fig. 3. As shown in Fig. 3(a), for a nanosphere with a diameter of 36 nm, two electron bunches, emitting upward and downward respectively, can be generated. Under the same initial volume, the nanofoil target with a transverse length of 20 nm and a longitudinal length of 50 nm can also generate a similar electronic distribution, as shown in Fig. 3(e). Comparing Figs. 3(a) and 3(e), it is clear that the angular spread of the emitting electrons is slightly smaller for the target geometries (3). After the summation along the Y axis, the results in Fig. 3(i) show that very similar electron spatial distribution can be obtained for the target geometries (2) and (3) with ultrasmall target size. Such similarity means that the target geometry under ultrasmall target size will not affect the final electron spatial distribution.

However, with the increasing total volumes, the targets with the same volumes and different geometries lead to a different evolution of electron spatial distribution. For nanosphere targets, increasing the diameter is equivalent to synchronously increasing the transverse and longitudinal size. The results in Figs. 3(b)–3(d) show that the angular spread of the emitting electrons keeps increasing with the increase of the target diameter. The number of electron bunches also keeps increasing. For nanofoil targets, the results in Figs. 3(f)–3(h) show that such a tendency develops more slowly. For the summation results in Figs. 3(i)–3(l), different tendencies have also emerged. Under a small target volume, the nanosphere target leads to a higher quantity in each electron bunch. When the target volume increases, the quantity in each electron bunch of the nanofoil targets will grow faster than that of the nanosphere targets.

The simulation results for the mass-limited nanoscale targets in Figs. 2 and 3 clearly show the different effects of the increase of the target transverse and longitudinal length to the finally obtained electronic distributions. The increase of the transverse length is not conducive to the improvement of the electron quantity in each bunch. Multiple electron bunches, as an adverse consequence, are also produced. Although multiple electron bunches will also appear when the longitudinal size increases to a large value, increasing the longitudinal size within a certain range can effectively improve the electronic quantity in a single electron bunch while the generation of multiple electron bunches is controlled. So to obtain an isolated electron bunch with a high quantity, it is an advantageous way to use a mass-limited target with a limited transverse size and a relatively large longitudinal size. Therefore, in the following paragraphs, our research will focus on the mass-limited nanofoil target with limited transverse size and large longitudinal size.

III. GENERATION OF ELECTRON BUNCHES DURING A LINEARLY POLARIZED LASER PULSE GRAZING PROPAGATED ALONG A NANOFOIL TARGET

In the following simulations, a linearly polarized laser pulse grazing propagated along a nanofoil target with a thickness smaller than the skin depth, as shown in Fig. 4(a). An initially ionized nanofoil target with 2000 nm in length and 20 nm in thickness is used. The target is located at $X \in [1600, 3600]$ nm, $Y \in [-10, 10]$ nm with an electron density of $n_e = 75n_c$, where n_c is the critical density. Noted that the electron density used in our simulations is smaller than that of the solid carbon, which ensures the target thickness is less than the skin depth c/ω_{pe}, where c is light speed and ω_{pe} is the plasma frequency. When the electrons in the target are ejected by the laser field, the left ions form the CSF. The continual electron ejection driven by the laser field will lead to an increasingly effective target length L_{eff} and increasing intensity of CSF. The other simulation parameters are the same as those in Sec. II.

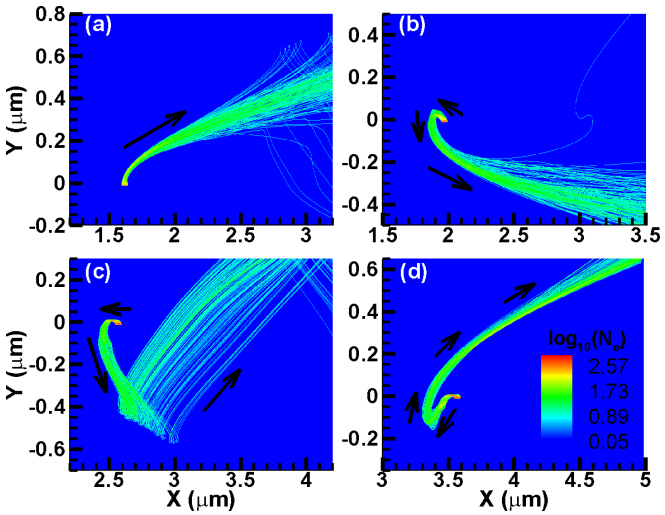

FIG. 5. (a) The trajectories for the electrons with initial x location within [1600, 1650] nm. (b) The trajectories for the electrons with initial x location within [1950, 2000] nm. (c) The trajectories for the electrons with initial x location within [2550, 2600] nm. (d) The trajectories for the electrons with initial x location within [3550, 3600] nm. The colorbar indicates the logarithm value of the electron spatial density with arbitrary units.

PIC simulations show that during the propagating of laser pulse along the nanofoil target, fanlike electron bunches can be periodically produced as in Fig. 4(b). As indicated by the black arrows, the electron bunches emit out in different directions. In many previous studies [1,3–5,18,43,44], similar electron bunches can be generated under different conditions. The shortest electron bunch duration (FWHM) in our simulations results is ∼47as, which is shown in Fig. 4(c).

To analyze the bunch generation mechanism in our simulations, the trajectories of the electrons with different initial X locations are obtained from the simulation results, as in Fig. 5. Through analyzing the trajectories in Fig. 5, the temporal and spatial evolution of the X component of velocity V_x and energy γ for the electrons with different initial x locations can be obtained as Fig. 6. Combining Figs. 5(a) and 6(a), they clearly show that the electrons located at the earliest part of the target, within [1600, 1650] nm, will be directly dragged out and pushed forward by the laser field. The emitting direction is shown as the black arrow in Fig. 5(a) denoting. Figure 6(e) shows that after ejecting from the target, these electrons will be concentrated within a very short time and then expand rapidly. After some electrons in a part of the target are ejected, the electrons located within [1950, 2000] nm have a different evolution process. As the black arrows in Fig. 5(b) and Fig. 6(b) indicate, the electrons initially move obliquely toward the $-X$ direction. Then they turn around and emit out obliquely downward. The evolution of electron energy in Fig. 6(f) shows that a similar concentration and expansion of electrons as in Fig. 6(e) will happen. But the electrons will be accelerated to a high energy. The final emitting directions in Figs. 5(a) and 5(b) are different, which can be explained by the evolution in the neighbor laser half cycles with opposite electric field E_y. When the electrons in a longer part of the target are ejected, the spatial evolution for the electrons with the initial X location within [2550, 2600] nm begins to change. As in Figs. 5(c) and 6(c), the initial parts of the electron trajectories are similar to those in Fig. 5(b). But the finally electron-emitting direction changes obliquely upward. Compared with Fig. 6(f), in Fig. 6(g) there is a second concentration of electrons which may lead to a second radiation pulse. At last, when almost all of the electrons are ejected, Figs. 5(d) and 6(d) show that the electrons initially located within [3550, 3600] nm move toward $-X$, $-Y$ direction for a longer distance than in Fig. 5(b). Then they turn around and emit out obliquely upward. The evolution of electron energy in Fig. 6(h) shows that the electrons will be concentrated for an obvious longer time and be accelerated to a much higher energy $\gamma \sim 50$. The electron trajectory evolutions and velocity evolutions shown in Figs. 5 and 6 mean that the electrons will be periodically dragged out and pushed obliquely upward and obliquely downward. This phenomenon leads to the fanlike electron bunches as in Fig. 4(b). The energy evolutions shown in Fig. 6 show that after ejected from the target, the electrons will be concentrated within a very short time and then expand rapidly. The later ejected electrons can acquire high energy before expanding.

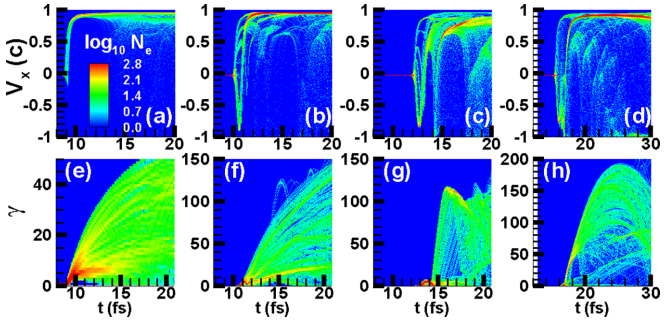

FIG. 6. The evolution of the X component of velocity V_x and energy γ for the electrons with initial x location within (a), (e) [1600, 1650] nm, (b), (f) [1950, 2000] nm, (c), (g) [2550, 2600] nm, and (d), (h) [3550, 3600] nm. The colorbar indicates the logarithm value of the electron spatial density with arbitrary units.

IV. NUMERICAL ANALYSIS ON THE ELECTRON MOTIONS UNDER THE INFLUENCE OF THE CSF AND LASER ELECTRIC FIELD

To analyze the detailed mechanism of the electron trajectory evolution, the electric field produced by the ions in the target can be drawn from our PIC simulation results. The two-dimensional spatial distribution of electric field E_x near the target is shown in Fig. 7(a). The one-dimensional distribution of the electric field E_x along the central axis of the target can also be drawn from the simulation results as the black dashed line in Fig. 7(b).

As the derivation in the Appendix of this paper shows, due to the symmetry of the target, the one-dimensional electric field distribution $E_x(L, S, r)$ along the target central axis ($Y = 0$), for a target with a length of L and thickness of S, can

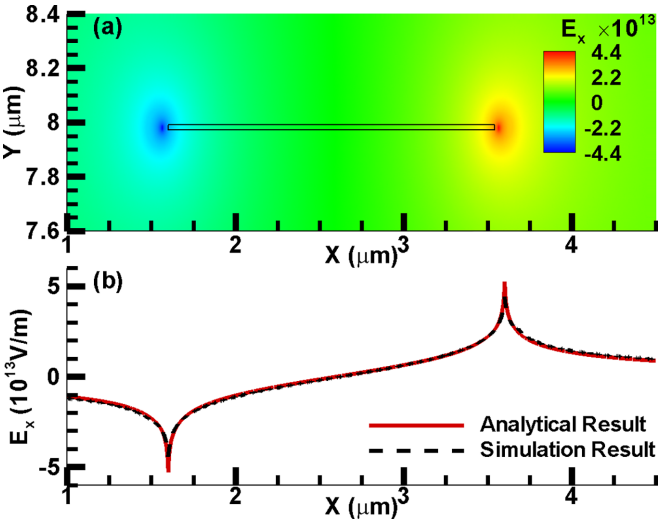

FIG. 7. (a) The two-dimensional spatial distribution of electric field E_x (V/m) near the target obtained from simulation results at $t = 12T$, where T is laser period. The rectangle denotes the outline of the target with $L = 2000$ nm, $S = 20$ nm, and $n_e = 75n_c$. (b) The one-dimensional distribution of the electric field E_x along the target central axis obtained from the simulation results and analytical formula Eq. (2).

be calculated using the formula

$$E_x(L, S, r) = \pm\left[F\left(\frac{r+L}{S/2}\right) - F\left(\frac{r}{S/2}\right)\right], \quad (1)$$

$$\pm\left[F\left(\frac{|x_0|+L/2}{S/2}\right) - F\left(\frac{|x_0|-L/2}{S/2}\right)\right], \quad (2)$$

where

$$F(y) = \frac{Sn_e}{2\pi\varepsilon_0}\left[y\arctan(1/y) + \frac{1}{2}\ln(1+y^2)\right]. \quad (3)$$

$r = |x_0| - L/2$ is the absolute distance from the observation point to the nearest target edge. x_0 is the x coordinate of the observation point. $+$ and $-$ correspond to $x_0 > L/2$ and $x_0 < -L/2$, respectively. It notes that Eq. (2) is only valid for $|x_0| > L/2$. When the observation point is placed inside the target, $|x_0| < L/2$, the electric field produced by a part of the target will counteract with each other. So this observation point can be considered as being affected by an equivalent volume charge with a length of $L' = 2|x_0|$ at a distance of $r' = L/2 - |x_0|$. Then by replacing the L and r in Eq. (1) by L' and r', the electric field for $|x| < L/2$ can be obtained from $E_x(L', S, r')$. What is more, Eq. (2) is only valid for the target with finite L, S, and infinite length along the Z axis, which is consistent with the 2D simulation case. The calculated result is shown as the red solid line in Fig. 7(b), where the numerically obtained result is consistent with the simulation result. From the results in Fig. 7, we can confirm that the charge separation field produced by the ionized target is mainly localized at the surface of the target. The electric field E_x at the right edge of the target points toward the $+X$ direction.

Further calculations using Eq. (2) show that the charge separation field E_x is in direct proportion to the effective target length L_{eff}. When the laser propagates along the target, the continuous ejection of the electrons from the target will lead to the continuously increasing effective target length L_{eff} as well as the corresponding charge separation field. So the electrons located at the different parts of the target are affected by the charge separation field with different intensities. The influence of the charge separation field on the electrons located at the earliest part of the target, $X \in [0, 50]$ nm, can be nearly ignored, for the very short L_{eff}. For the electrons with increasing X coordinates, the influence of the charge separation field keeps increasing for the increasing L_{eff}.

Considering the electrons in the target are affected by both the laser field and the charge separation field, it is necessary to qualitatively analyze the different roles of the two fields in the electron accelerating process first. In the beginning, the X component of the charge separation field accelerates the electron toward the $-X$ direction. The Y component of electron velocity v_y is much less than the light speed at this time, so the Lorentz force along the X axis produced by laser magnetic field, in direct proportion to $\mathbf{v}_y \times \mathbf{B}$, can be ignored. For the laser polarized along the Y axis, the laser field is much larger than the Y component of the charge separation field E_y, the effects of the charge separation field along the Y axis can also be ignored. Along the Y axis, the electrons will be accelerated by the Y component of the laser field and leave the effecting region of the charge separation field after a very short moment. Considering the charge separation field is highly localized at the surface of the target, the effective affecting time of the charge separation field is ultrashort. So the corresponding influences of the charge separation field on the electrons can be considered as an abrupt shock toward the $-X$ direction. This shock can be simplified as the initial electron energy $\gamma_0 = 1\sqrt{1-(v_0/c)^2}$ and the electron initial velocity $-v_0$ toward the $-X$ direction.

All of the electrons can be considered to be initially located at the right edge of a fictitious target, where the effective target length L_{eff} keeps increasing during the continuous electron ejection from the target. When a free electron is accelerated by the charge separation field shown in Fig. 7 from the right edge to the center of the target, it can acquire the maximum initial energy from the charge separation field. The maximum initial energy can be calculated through the numerical integration

$$W = (\gamma_0 - 1)m_e c^2 = \int_0^{L/2} eE_x(L, S, r(x'))dx', \quad (4)$$

where γ_0 is the initial Lorentz factor of the electron, m_e is the electron mass, e is the charge of electron, $E_x(L, S, r(x'))$ is the charge separation field defined by Eq. (2). According to Eq. (2), the relation between the electron initial Lorentz factor and the target lengths L can be obtained as Fig. 8(a). These results show that the electron initial Lorentz factor is in direct proportion to L. It notes that the electrons always leave the effective region of the charge separation field quickly and early due to transverse motion driven by the laser field. So the electron acceleration distance is always shorter than $L/2$. As a result, the integration results from Eq. (4) always overestimate the electron initial Lorentz factor. But considering γ_0 always increases from 1 to a higher value for the increasing effective target length L_{eff}, the maximum Lorentz factor can always be

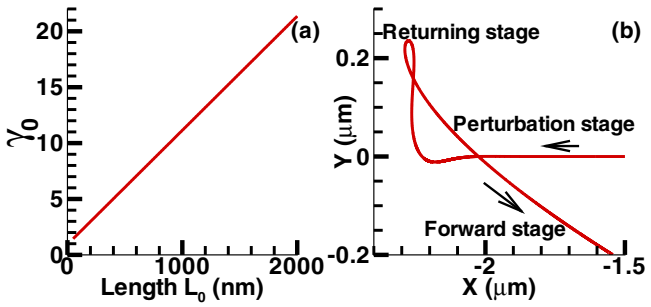

FIG. 8. (a) The relation between the effective target length L_{eff} and maximum electron initial Lorentz factor $\boldsymbol{\gamma_0}$. (b) The trajectory for an electron with initial Lorentz factor $\gamma_0 = 2.46$ calculated using Eq. (5).

achieved for a certain L_{eff}. So using the maximum Lorentz factor calculated by Eq. (4) as the electron initial Lorentz factor is acceptable.

Under the above simplifications, the interaction between a relativistic laser pulse and an electron at the right edge of the target can be numerically calculated from the relativistic electron motion equation

$$\frac{d\mathbf{P}}{dt} = \frac{d(\gamma m_e \mathbf{v})}{dt} = -e(\mathbf{E} + \mathbf{v} \times \mathbf{B}), \tag{5}$$

where $\mathbf{P} = \gamma m_e \mathbf{v}$ is the electron momentum, γ is the normalized transient energy of the electron, $\mathbf{v} = (v_\parallel, v_\perp, 0)$ is the electron velocity (with parallel and perpendicular velocity components, respectively), $\mathbf{E}$ and $\mathbf{B}$ are the electric and magnetic fields associated with the laser. The temporal profile of the laser electric field can be given by the formula

$$E(t) = E_0 \cos\left[-\frac{2\pi c}{\lambda}(t - x/c) + \phi_0\right] e^{-\frac{64\ln 2(t-x/c)^2}{\sigma^2} - y^2/\tau^2}, \tag{6}$$

with a pulse duration $\sigma = 5\lambda/c$, transverse width $\tau = 3\lambda$, wavelength $\lambda = 800$ nm, and initial phase $\phi_0 = 0$. The normalized laser field a_0 is 100. For one electron with initial energy $\gamma_0 = 2.46$, the electron trajectory is obtained as in Fig. 8(b). In the calculations, all of the electrons are released at the same initial position $X = 0$ and the same initial time t = 0. The laser parameters are the same as those in the previous PIC simulations. The calculated trajectory in Fig. 8(b) shows that for the electron with an initial velocity towards the $-X$ direction, its acceleration process affected by a relativistic laser pulse moving toward $+X$ direction can be divided into three stages: The perturbation stage, the returning stage, and the forward stage.

To analyze the generation mechanisms of the three stages, the electron position $X(t)$ and $Y(t)$, velocity $V_x(t)$ and $V_y(t)$, acceleration $a_x(t)$ and $a_y(t)$, radiation power $P(t)$, and the electron moving direction $\theta(t)$ are calculated as shown in Fig. 9. Combining Figs. 9(a) and 9(b), it is clear that during the perturbation stage, the laser field will act as a perturbation. The electron initial velocity V_x cannot be completely reduced to zero by the laser field. At the transient moment indicated by the black dashed line, V_x is restored to its initial value. Next, when the electron moves into the next laser half cycle, the

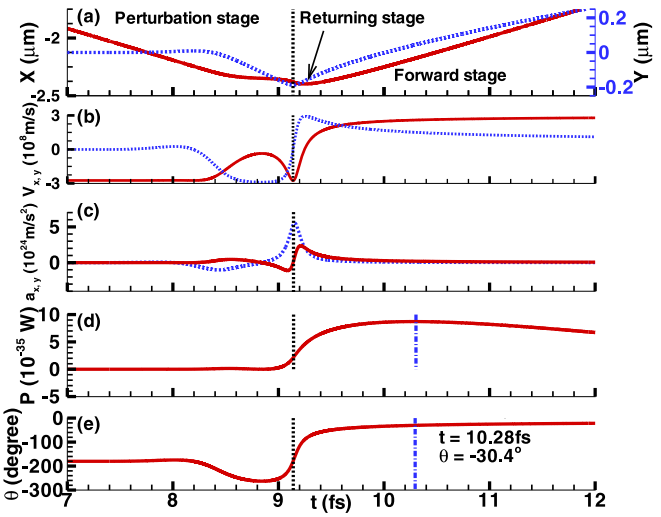

FIG. 9. From the trajectory in Fig. 8(b), the (a) X and Y position, (b) electron velocity, (c) acceleration, (d) radiation power, and (e) electron moving direction θ related to time can be obtained. Red solid lines in (a)–(c) are for the X component, blue dashed lines in (a)–(c) are for the Y component.

higher laser electric field can completely reduce the electron's initial velocity to zero and make the electron turn around. This ultrashort time interval can be defined as the returning stage. The returning moment is always close to the peak of the laser electric field. So as shown in Fig. 9(c), quickly after the electron returns, the electron accelerations will reach the maximum value.

For the electron-emitting direction keeps changing, it is necessary to find a typical moment to characterize the emitting direction. The moment, when the radiation power reaches the maximum, can reflect the central emitting direction of the radiations generated by the electrons, which can be used as a signpost. The radiation power can be calculated from the electron trajectory and velocity [45]

$$P(t) = \frac{2}{3}\frac{e^2|\mathbf{v}|^2}{c^3}\gamma^4, \tag{7}$$

where P is the radiation power, and .$\mathbf{v}$ is the electron acceleration. When the equilibrium between the increasing electron energy γ and the decreasing acceleration is achieved, the radiation power $P(t)$ will reach the extreme value, as indicated by the blue dash-dot line in Fig. 9(d). Using the formula $\theta = \arctan(V_y/V_x)$, the intersection angle of the electron moving direction to the $+X$ direction can be obtained as Fig. 9(e). At the moment $t = 10.28$ fs when the radiation power $P(t)$ reaches the extreme value, the blue dash-dot line in Fig. 9(e) indicates that θ is $-30.4°$. This emitting angle is consistent with the trajectories in Fig. 6(b). For simplification in the following paragraphs, the moments when the electrons return and the radiation power reaches the extreme values are defined as the returning points and extreme points, respectively.

Similar emitting angle analysis in Fig. 9 can be conducted for electrons with different initial energy, which can reflect the generating process of the electron bunches in Fig. 2(b). For electrons with initial energy γ_0 ranging from 1.01 to 21, the emitting angles $\theta = \arctan(V_y/V_x)$ at the first, second and

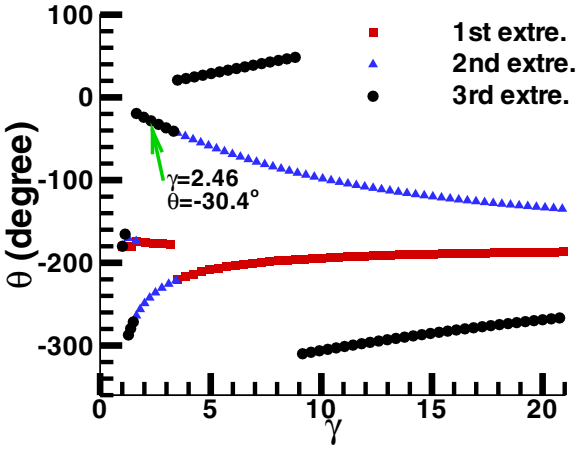

FIG. 10. The relation between the electron's initial kinetic energy γ_0 and the electron moving direction at the first, second, and third extreme points.

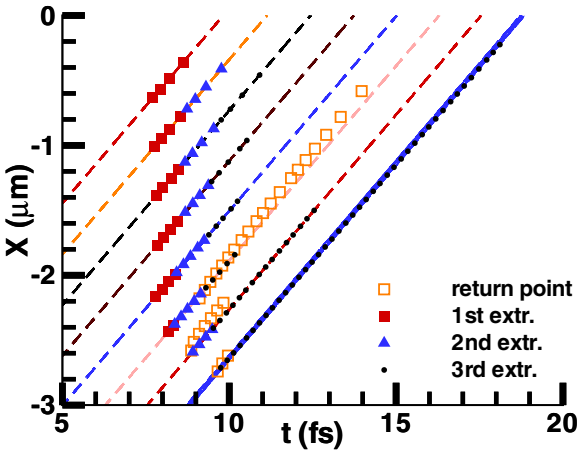

FIG. 11. The returning points (black circle) and the extreme points (orange square). The four lines are the X position evolution of the laser electric peaks. To prevent the symbols from overlapping with each other, many overlapped symbols are omitted in this figure. The black arrows denote the increase of γ_0.

third extreme points are shown in Fig. 10. This figure clearly shows that for the increasing γ_0, the electron bunches will alternately emit out toward two opposite directions. Electrons with similar initial energy and emitting direction will form several bunches emitting out toward different directions. What is more, for the first, second, and third extreme points, the emitting directions have different evolution tendencies. For low initial energy γ_0, within three ranges such as $\gamma_0 = 1.01 \sim 3.49$ for the first extreme points, $\gamma_0 = 1.01 \sim 1.63$ for the second extreme points and $\gamma_0 = 1.01 \sim 1.27$ for the third extreme points, the emitting directions are around $-180°$, which is consistent with the electron's initial moving directions. This phenomenon means that the radiation corresponding to these points occurs within the perturbation stage. The tendencies are different for higher initial energy γ_0. Despite the points around $\theta \sim -180°$, the other extreme points will alternately jump toward two opposite directions. For the electron with initial energy $\gamma_0 = 2.46$, Fig. 10 shows that the radiation emitting toward $\theta = -30.4°$ comes from the contribution of the third extreme point.

For the electron trajectories obtained in the semianalytical analyses, the spatial and temporal relationship between the electron trajectories and laser field can also be analyzed to explore the electron-bunching process. In the calculations, all of the electrons are released at the same initial position and the initial time. The $X(t)$ coordinates of the returning points and the first, second, and third extreme points for the trajectories of the electrons with initial energy γ_0 from 1.01 to 21 are scattered plotted in Fig. 11. In this figure, the X position evolution of the laser electric peaks is recorded as the eight lines, which act as a position datum. The blue solid line corresponds to the maximum peak of the laser field. When γ_0 is increased from 1.1 to 21, the returning points and the extreme points will gradually shift from the leading peaks of the laser electric field to the following peaks. The different γ_0 ranges in each line are shown in Table I. This tendency means that the electrons are divided into several groups based on their initial energy and emitting out within different laser half cycles. During the oscillating in the laser field, the electrons will generate several radiation pulses. For electrons with higher initial energy, a longer stopping distance in the laser field is required, which leads to the sudden jumps of radiation extreme points with the increasing γ_0. For an electron with a certain γ_0, the corresponding first, second, and third radiation extreme points jump between the adjacent laser half-cycles. The radiation generated before the electron returning point, shown as the points within the left five lines in Fig. 11 and the 1 to 5 columns in Table. I, can be considered as the radiation within the perturbation stage. After the electrons return, the deviation of the perturbation stage will lead to the radiation emitting toward the direction deviating from $\theta \sim -180°$. The angular analysis in Fig. 10 can support these conclusion. A similar analysis in Fig. 9 can be conducted for the electron trajectories obtained from the PIC simulation results. Based

TABLE I. The ranges of electron initial energy γ_0 for the return points, first extreme points, second extreme points, and third extreme points in each line in Fig. 11.

	Number of laser half-cycles							
	1	2	3	4	5	6	7	8
Return point	null	null	null	null	null	1.01 ∼ 1.8	1.81 ∼ 12.06	12.07 ∼ 21
1st extreme	1.01 ∼ 1.04	1.05 ∼ 1.12	1.13 ∼ 1.27	1.28 ∼ 1.63	1.64 ∼ 3.49	3.5 ∼ 21	null	null
2nd extreme	null	1.01 ∼ 1.04	1.05 ∼ 1.12	1.13 ∼ 1.27	1.28 ∼ 1.63	1.64 ∼ 3.49	3.5 ∼ 21	null
3rd extreme	null	null	1.01 ∼ 1.04	1.05 ∼ 1.12	1.13 ∼ 1.27	1.28 ∼ 1.63	1.64 ∼ 3.49	3.5 ∼ 21

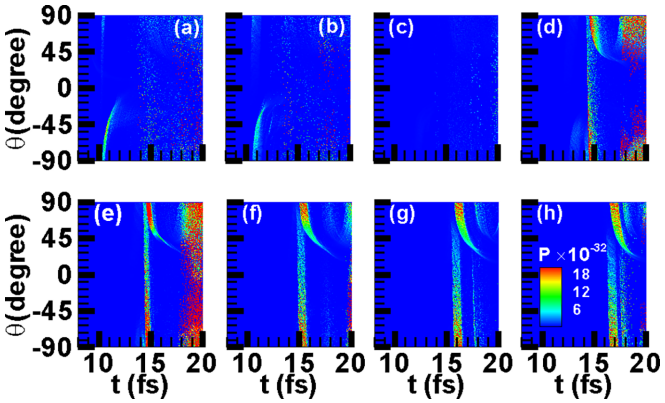

FIG. 12. The superimposed radiation evolution arrays $P(\theta, t)$ (a.u.) for electrons within the initial location in the target of (a) 1600 to 1850 nm, (b) 1850 to 2100 nm, (c) 2100 to 2350 nm, (d) 2350 to 2600 nm, (e) 2600 to 2850 nm, (f) 2850 to 3100 nm, (g) 3100 to 3350 nm, (h) 3350 to 3600 nm.

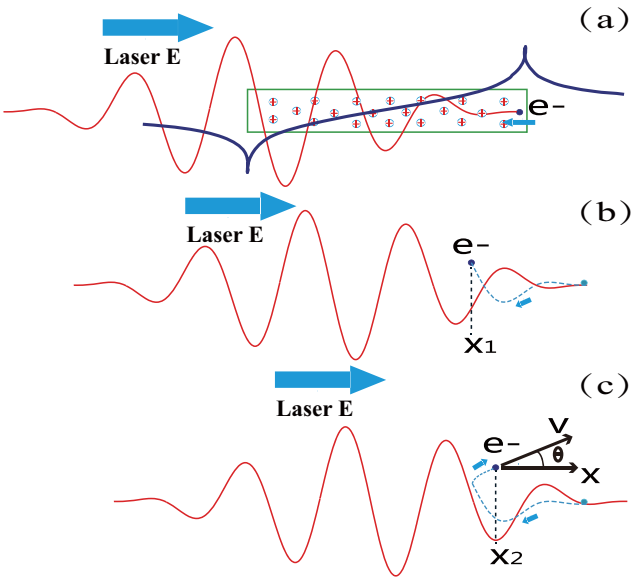

FIG. 13. The schematic drawing of the interaction between the relativistic laser pulse and nanoscale target. The angle between the electron moving direction and $+X$ direction is defined as θ.

on the electron trajectories obtained from the PIC simulation results, the critical frequency ω_c and critical energy E_c can be estimated using Jackson's formulas [45]: $\omega_c = 3/2\gamma^3(c/\rho)$ and $E_c = \hbar\omega_c$. The analysis shows that for most of the electrons in the target, the peaks of the critical frequency ω_c are ranged between $1 \sim 2 \times 10^{19}$/s, which means the radiation will have critical energy E_c ranged between 6.5 ∼13 keV. To reflect the moving and radiation tendency of a large number of electrons with different initial locations in the target, the temporal evolution of the electron moving direction $\theta(t)$ and radiation power $P(t)$ can be calculated from the electron trajectories. The relation between the radiation power P and θ, t can be obtained as a two-dimensional radiation evolution array $P(\theta, t)$. The target with a length of 2000 nm is divided into 8 sections. Each section has a length of 250 nm. For the electrons in the same section, their radiation evolution arrays $P(\theta, t)$ can be linearly superimposed, leading to Fig. 12.

Compared with Fig. 9, Fig. 12 reflects the moving tendency for all of the electrons in the target. For Figs. 12(a) and 12(b), the electrons are located from 1600 nm to 2100 nm. The corresponding radiation is generated in the first laser half cycle, which emits out mainly toward a large angle (90 or −90 degrees). From Figs. 12(a) to 12(b), the electrons located afterward will be ejected later, leading to the gradual delay of radiation. Fig. 12(c) is the transition regime. The radiation intensity for the electrons located at 2100 to 2350 nm is quite weak. For Figs. 12(d)–12(h), the electrons with higher initial energy penetrate the next laser half cycle. Due to the different electron acceleration processes, the generated radiation emits out in a different direction at an obviously delayed time.

Based on our simulations and calculation results, the electron acceleration processes when an ultraintense, linearly polarized laser pulse propagates along a nanoscale target can be revealed and schematically shown as the several steps in Fig. 13. In Fig. 13(a), when the laser propagates along the target, the continuous ejection of the electrons on the target form a continuously increasing effective target length and corresponding charge separation field, which is highly localized around the surface of the target. The X component of the charge separation field E_x is shown as the blue thick line. An electron at the right edge of the target will be accelerated by E_x, whose effect can be considered as an abrupt shock towards the $-X$ direction and an initial electron velocity $-v_0$. For a longer effective target, the higher charge separation field will lead to electrons with higher initial kinetic energy. Then as in Fig. 13(b) the electron is periodically accelerated and decelerated in each half cycle of the laser electric field. If the initial velocity $-v_0$ cannot be reduced to zero near the peak of the laser electric field, the remaining part of the current half-cycle cannot make the electron stop and turn around. Then the electron enters the next half-cycle, where the peak intensity of the laser electric field is higher. If the laser field intensity is high enough, then the electron will stop at the position x_1. Finally, for the last step as in Fig. 13(c), the electron will be pushed toward the obliquely $+X$ direction by the laser field. When the peak of the laser electric field catches up with the electron, at x_2, the intense laser electric field will lead to violent acceleration. The radiation intensity also reaches an extreme value. During the continuous electron ejection from the target, the electrons located at the different parts of the target will acquire different initial energy in the charge separation field. Then according to the different initial energy, all of the electrons in the target are divided into several groups and accelerated within different laser half cycles. The electrons in the same group form a fan-like attosecond electron bunch. By adjusting the length of the nanoscale target, the number of attosecond electron bunches can be naturally controlled.

V. CONTROLLING THE NUMBER OF ATTOSECOND PULSES THROUGH ADJUSTING THE TARGET LENGTH

The previous studies [18] have shown that the interaction between dense nanobunches of electrons and relativistic laser pulse can lead to attosecond radiation pulses through the CSE

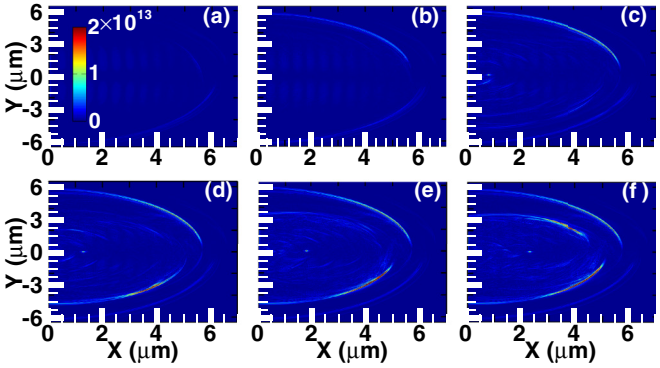

FIG. 14. The obtained X component of electric fields E_x(V/m) for targets with the length of (a) 200 nm, (b) 400 nm, (c) 800 nm, (d) 1200 nm, (e) 1600 nm, (f) 2000 nm, at $t = 12T$. The colorbar indicates the intensity of the electric field with arbitrary units.

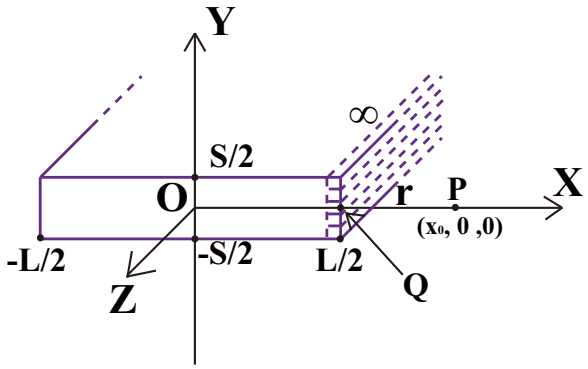

FIG. 15. The coordinate system and target position.

mechanism. In our simulations, attosecond radiation pulses will also be generated through the CSE mechanism. To exhibit the influence of the target length on the number of attosecond pulses, similar simulations as in Fig. 6 were conducted with the same parameters except for a little larger target thickness $\mathbf{S} = 40$ nm. The obtained X component of the electric fields E_x are shown in Fig. 14, where the laser electric field is filtered. The figures clearly show that when the target length is reduced from 2000 to 200 nm, the number of attosecond pulses is reduced synchronously. When the target length is shorter than 400 nm, toward the obliquely downward, an isolated attosecond electron bunch may be directly generated even for a multicycle relativistic laser pulse. Then the further length reduction from 400 to 200nm will lead to the reduction of radiation intensity.

VI. OUTLOOK AND CONCLUSION

For mass-limited nanoscale targets under the illumination of a relativistic ultrafast laser pulse, the comparisons of the finally obtained electronic distributions for three different target geometries can lead to the conclusion that for a nanofoil target, limiting the transverse target size to a small value and increasing the longitudinal target size to a certain extent can significantly improve the total electron number in a single bunch. Then the mechanism for the periodical generation of relativistic attosecond electron bunches when an ultraintense, linearly polarized laser pulse grazing propagates along a nanofoil target was explored. Through analyzing the subfemtosecond electronic dynamics during the electron-bunching process, it confirms that the charge separation field produced by the ionized target plays a key role in the generation of electron bunches. The electron's initial energy, the following evolution process in the laser field and the final emitting direction can be directly determined by the intensity of the charge separation field. According to the different initial energy, all of the electrons in the target are divided into several bunches and accelerated within different laser half cycles. By adjusting the length of the nanoscale target, the number of attosecond radiation bunches can be directly controlled. When the target length is short enough, an isolated attosecond pulse may be directly generated.

ACKNOWLEDGMENTS

The authors acknowledge support from the Science Challenge Program (Project No. TZ2017005), the NSAF (Grant No. U1630246), the Presidential Foundation of China Academy of Engineering Physics (Grant No. 2014-1-017), and the National Key R&D Program (Grant No. 2016YFA0401100).

APPENDIX

According to Coulomb's Law and the principle of superposition, the electric field around a volume charge can be obtained by evaluating the integral

$$E(\mathbf{x}) = \frac{n_i}{4\pi\varepsilon_0}\int D(\mathbf{x}')\frac{\mathbf{x}-\mathbf{x}'}{|\mathbf{x}-\mathbf{x}'|^3}d^3x, \tag{A1}$$

where $\mathrm{D}(\mathbf{x}')$ is the dimensionless electronic spatial distribution, n_i is the amplitude of the charge density (charge/volume).

The nanofoil target used in our 2D PIC simulations can be considered as a volume charge with finite length L, finite height S, and infinite thickness. The coordinate system is shown in Fig. 15. The original point O is placed at the center of the target. An observation point is placed at P with the coordinate of $(x_0, 0, 0)$, which is placed at the central axis. For an arbitrary point Q placed in the volume charge, the distance between P and Q is r.

The volume charge can be divided into many surface charges. Each surface charge can be divided into many line charges perpendicular to the XY plane. So to obtain the electric field at point P produced by the volume charge, the integral Eq. (A1) can be divided into several corresponding steps.

First, for an observation point P placed at the right side of the target, with $x_0 \geqslant L/2$, the dimensionless electric field at point P produced by a wire charge passing through point Q is

$$I(R) = \frac{2}{R}\mathbf{e}_r, \tag{A2}$$

where $\mathbf{e}_r$ is a unit vector directing from point Q to point P, R is the length of QP. When point Q is placed at $(L/2, 0, 0)$, $R = r = |x_0| - L/2$. Then for a surface charge in the target containing many wire charges, the Y component of the electric field is reduced to zero due to the symmetry of the surface charge. At point P, only the X component of the electric field

is nonzero. The integral of these wire charges will lead to the electric field produced by the surface charge as

$$\int_{-S/2}^{+S/2} ds \frac{2}{R}\cos\theta \tag{A3}$$

$$= \int_{-S/2}^{+S/2} \frac{2rds}{r^2+s^2} \tag{A4}$$

$$= 4\arctan\left(\frac{S/2}{r}\right), \tag{A5}$$

where $\cos\theta = r/\sqrt{r^2+s^2}$. Finally, the X component of the electric field at point P produced by the whole volume charge can be calculated through the integral for all of the surface charges as

$$E_x(L,S,r) \tag{A6}$$

$$= \frac{n_e}{4\pi\varepsilon_0}\int_r^{r+L} dr' 4\arctan\left(\frac{S/2}{r'}\right) \tag{A7}$$

$$= \frac{n_e}{\pi\varepsilon_0}\cdot S/2\int_{r/(S/2)}^{(r+L)/(S/2)} dy \arctan\left(\frac{1}{y}\right) \tag{A8}$$

$$= F\left(\frac{r+L}{S/2}\right) - F\left(\frac{r}{S/2}\right), \tag{A9}$$

where

$$F(y) = \frac{Sn_e}{2\pi\varepsilon_0}\left[y\arctan(1/y) + \frac{1}{2}\ln(1+y^2)\right]. \tag{A10}$$

When point P is placed at the left side of the target, $x_0 < -L/2$, the symmetry will lead to

$$E_x(L,S,r) \tag{A11}$$

$$= -\left[F\left(\frac{r+L}{S/2}\right) - F\left(\frac{r}{S/2}\right)\right], \tag{A12}$$

When point P is placed in the target, the electric field produced by the surface charges at the left side and right side of point P will counteract each other. The electric field at point P can be considered to be produced by an equivalent volume charge with a length of $2|x_0|$ and a distance of $r = L/2 - |x_0|$. So the electric field is $E_x(2|x_0|, S, L/2-|x|)$ for $0 < x_0 < L/2$, and $-E_x(2|x_0|, S, L/2-|x_0|)$ for $-L/2 < x_0 < 0$.

Finally, when $|x_0| \geqslant L/2$, the X component of the electric field E_x along the target central axis for the target used in our simulations has a formula

$$E_x(L,S,|x_0|) = \pm\left[F\left(\frac{|x_0|+L/2}{S/2}\right) - F\left(\frac{|x_0|-L/2}{S/2}\right)\right]. \tag{A13}$$

When $|x_0| < L/2$, the electric field can be calculated using Eq. (A13) with replacing L to $2|x_0|$ and r to $L/2-|x_0|$.

[1] N. Naumova, I. Sokolov, J. Nees, A. Maksimchuk, V. Yanovsky, and G. Mourou, Phys. Rev. Lett. **93**, 195003 (2004).
[2] V. V. Kulagin, V. A. Cherepenin, M. S. Hur, and H. Suk, Phys. Rev. Lett. **99**, 124801 (2007).
[3] T. V. Liseykina, S. Pirner, and D. Bauer, Phys. Rev. Lett. **104**, 095002 (2010).
[4] S. Cousens, B. Reville, B. Dromey, and M. Zepf, Phys. Rev. Lett. **116**, 083901 (2016).
[5] D. E. Cardenas, T. M. Ostermayr, L. Di Lucchio, L. Hofmann, M. F. Kling, P. Gibbon, J. Schreiber, and L. Veisz, Sci. Rep. **9**, 7321 (2019).
[6] F. Quéré, C. Thaury, P. Monot, S. Dobosz, Ph. Martin, J.-P. Geindre, and P. Audebert, Phys. Rev. Lett. **96**, 125004 (2006).
[7] C. Thaury, F. Quéré, J.-P. Geindre, A. Levy, T. Ceccotti, P. Monot, M. Bougeard, F. Réau, P. d'Oliveira, P. Audebert *et al.*, Nat. Phys. **3**, 424 (2007).
[8] R. Lichters, J. Meyer-ter-Vehn, and A. Pukhov, Phys. Plasma **3**, 3425 (1996).
[9] S. V. Bulanov, N. M. Naumova, and F. Pegoraro, Phys. Plasmas **1**, 745 (1994).
[10] P. Gibbon, Phys. Rev. Lett. **76**, 50 (1996).
[11] T. Baeva, S. Gordienko, and A. Pukhov, Phys. Rev. E **74**, 046404 (2006).
[12] B. Dromey, Nat. Phys. **2**, 456 (2006).
[13] B. Dromey, S. Kar, C. Bellei, D. C. Carroll, R. J. Clarke, J. S. Green, S. Kneip, K. Markey, S. R. Nagel, P. T. Simpson *et al.*, Phys. Rev. Lett. **99**, 085001 (2007).
[14] A. Tarasevitch, K. Lobov, C. Wunsche, and D. von der Linde, Phys. Rev. Lett. **98**, 103902 (2007).
[15] M. Zepf, Plasma Phys. Contr. F. **49**, B149 (2007).
[16] D. an der Brügge and A. Pukhov, Phys. Plasmas **17**, 033110 (2010).
[17] A. Pukhov, D. an der Brügge, and I. Kostyukov, Plasma Phys. Control. Fusion **52**, 124039 (2010).
[18] B. Dromey, S. Rykovanov, M. Yeung, R. Hörlein, D. Jung, D. C. Gautier, T. Dzelzainis, D. Kiefer, S. Palaniyppan, R. Shah *et al.*, Nat. Phys. **8**, 804 (2012).
[19] B. Dromey, S. Cousens, S. Rykovanov, M. Yeung, D. Jung, D. C. Gautier, T. Dzelzainis, D. Kiefer, S. Palaniyppan, and R. Shah, New J. Phys. **15**, 015025 (2013).
[20] U. Teubner and P. Gibbon, Rev. Mod. Phys. **81**, 445 (2009).
[21] T. Popmintchev, M.-C. Chen, P. Arpin, M. M. Murnane, and H. C. Kapteyn, Nat. Photon. **4**, 822 (2010).
[22] S. A. Aseyev, Y. Ni, L. J. Frasinski, H. G. Muller, and M. J. J. Vrakking, Phys. Rev. Lett. **91**, 223902 (2003).
[23] G. L. Yudin, A. D. Bandrauk, and P. B. Corkum, Phys. Rev. Lett. **96**, 063002 (2006).
[24] A. H. Zewail, Science **242**, 1645 (1988).
[25] K. J. Gaffney and H. N. Chapman, Science **316**, 1444 (2007).
[26] A. H. Zewail, Science **328**, 187 (2010).
[27] C. I. Blaga, J. L. Xu, A. D. DiChiara, E. Sistrunk, K. K. Zhang, P. Agostini, T. A. Miller, L. F. DiMauro, and C. D. Lin, Nature (London) **483**, 194 (2012).
[28] M. Y. Ivanov, Nature (London) **483**, 162 (2012).
[29] J. Itatani, F. Quéré, G. L. Yudin, M. Yu. Ivanov, F. Krausz, and P. B. Corkum, Phys. Rev. Lett. **88**, 173903 (2002).
[30] F. Lindner, M. G. Schätzel, H. Walther, A. Baltuška, E. Goulielmakis, F. Krausz, D. B. Milošević, D. Bauer, W. Becker, and G. G. Paulus, Phys. Rev. Lett. **95**, 040401 (2005).

[31] J. A. Wheeler, A. Borot, S. Monchocé, H. Vincenti, A. Ricci, A. Malvache, R. Lopez-Martens, and F. Quéré, Nat. Photon. **6**, 829 (2012).
[32] H. Vincenti and F. Quéré, Phys. Rev. Lett. **108**, 113904 (2012).
[33] M. Yeung, B. Dromey, S. Cousens, T. Dzelzainis, D. Kiefer, J. Schreiber, J. H. Bin, W. Ma, C. Kreuzer, J. Meyer-ter-Vehn, M. J. V. Streeter, P. S. Foster, S. Rykovanov, and M. Zepf, Phys. Rev. Lett. **112**, 123902 (2014).
[34] G. J. Ma, Phys. Plasmas **22**, 033105 (2015).
[35] M. Yeung, S. Rykovanov, J. Bierbach, L. Li, E. Eckner, S. Kuschel, A. Woldegeorgis, C. Rödel, A. Sävert, G. G. Paulus *et al.*, Nat. Photon. **11**, 32 (2017).
[36] M. Blanco and M. T. Flores-Arias, Opt. Express **25**, 13372 (2017).
[37] X. R. Xu, Y. X. Zhang, H. Zhang, H. Y. Lu, W. M. Zhou, C. T. Zhou, B. Dromey S. P. Zhu, M. Zepf, X. T. He, and Q. Bin, Optica **7**, 355 (2020).
[38] L. D. Lucchio and P. Gibbon, Phys. Rev. Acce. and Beams **18**, 023402 (2015).
[39] V. Horný and L. Veisz, Plasma Phys. Control. Fusion **63**, 125025 (2021).
[40] L. X. Hu, T. P. Yu, Z. M. Sheng, J. Vieira, D. B. Zou, Y. Yin, P. McKenna, and F. Q. Shao, Sci. Rep. **8**, 7282 (2018).
[41] J. F. Ong, P. Ghenuche, and K. A. Tanaka, Phys. Rev. Res. **3**, 033262 (2021).
[42] C. Nieter and J. R. Cary, J. Comput. Phys. **196**, 448 (2004).
[43] H.-Z. Li, T.-P. Yu, L.-X. Hu, Y. Yin, D.-B. Zou, J.-X. Liu, W.-Q. Wang, S. Hu, and F.-Q. Shao, Opt. Express **25**, 21583 (2017).
[44] Y. X. Zhang, B. Qiao, X. R. Xu, H. X. Chang, H. Zhang, H. Y. Lu, M. Y. Yu, C. T. Zhou, S. P. Zhu, and X. T. He, Phys. Plasmas **24**, 123119 (2017).
[45] J. D. Jackson, *Classical Electrodynamics* (Wiley, New York, NY, 1999).